RSC Advances

PAPER

View Article Online
View Journal | View Issue

Cite this: *RSC Adv.*, 2017, **7**, 19019

The synergetic effect of dual co-catalysts on the photocatalytic activity of square-like WO_3 with different exposed facets

Huihua Gong, Yue Cao, Yifeng Zhang, Yu Zhang, Kewei Liu, Hongmei Cao and Hongjian Yan *

Received 25th January 2017
Accepted 24th March 2017

DOI: 10.1039/c7ra01149k

rsc.li/rsc-advances

Here we report the controlled selective deposition of Pt and PbO_x dual-cocatalysts on the edged (200) and (020) facets and the main (002) facets of square-like WO_3 nanoplates, respectively. The remarkably enhanced photocatalytic activities were observed for such assembled photocatalysts in photocatalytic water oxidation. The superior performance can be attributed to not only the light-induced preferential flow of photogenerated electrons and holes onto different facets of the square-like WO_3, thus leading to the reduction and oxidation reactions taking place on the corresponding edged and major top facets, but also the selective deposition of suitable oxidation and reduction cocatalysts onto the needed facets of square-like WO_3 to reduce the charge recombination and catalyze the redox reactions. These findings will be promising and intriguing for designing high efficiency WO_3 system for visible light water splitting.

1. Introduction

Sustainable solar energy for the clean chemical energy (renewable energy sources) from H_2 and O_2 conversion using photocatalytic water splitting under visible light is one of the promising approaches to address the environmental issues and global energy shortage crisis.[1–3] Tungsten oxide (WO_3), an exceptionally important n-type visible-light semiconductor material with a narrow band gap of 2.4–2.8 eV, has attracted much attention in the field of photocatalysis due to its excellent electron transport properties and good resilience to photocorrosion effects in aqueous solution.[2,4–7] However, pure WO_3 is not an efficient photocatalyst due to the rapid recombination of photogenerated charge carriers and narrow photo-absorption range.[8] Cocatalysts play a significant role because they can serve as the active sites for the water splitting process and trap the photoexcited electrons and holes to improve the charge-separation.[9–15] It has been reported that selective deposition of suitable dual-cocatalysts (oxidation cocatalysts and reduction cocatalysts) on corresponding sites of semiconductor-based crystals (*e.g.*, $BiVO_4$, TiO_2, $SrTiO_3$, $PbTiO_3$) resulted in a remarkable enhanced photocatalytic performance due to the spatial separation of the photogenerated charges between different facets and the synergetic effect of dual-cocatalysts deposited onto the needed facets.[13,16–22] Our recent research works revealed that the square-like WO_3 nanoplates with Pt loaded mainly on dominant facets shows higher photocatalytic activity than that with Pt loaded on the edged facets due to light-induced charge separation between different facets of square-like WO_3.[23] However, the activity difference is not very big owe to that platinum particles were not effective oxidation reaction promoters for promoting O_2 evolution on the dominant (002) facets of square-like WO_3. Therefore, the selective deposition of suitable cocatalysts on the needed facets of square-like WO_3, particularly loading suitable oxygen-generation promoters on the dominant (002) facets to stress the surface recombination of charge carriers and thus improve photocatalytic performance is feasible and urgent based on the charge separation between different facets.

In this work, we have successfully prepared $Pt/PbO_x/WO_3$ by using a two-step photodeposition method. PbO_x nanoparticles as water oxidation cocatalyst were selectively deposited on the dominant (002) facets of square-like WO_3, while Pt as reduction cocatalyst were preferentially deposited on the minor (020) and (200) facets of square-like WO_3. The prepared $Pt/PbO_x/WO_3$ photocatalyst exhibits a significantly increased photocatalytic O_2 evolution rate in the presence of Ag^+ as sacrifice agent, exceeding that of WO_3 deposited with single PbO_x or Pt cocatalyst. The superior performance can be attributed to the intrinsic nature of charge separation between the different facets of WO_3, together with the co-loading of both Pt and PbO_x on reduction facets and oxidation facets of WO_3 to capture photogenerated electrons and holes and then reduce the charge recombination.

2. Experimental

2.1 Preparation of catalysts

2.1.1 Fabrication of square-like WO_3 nanoplates. All chemical reagents were of analytical grade and were used

College of Chemistry, Sichuan University, P. R. China. E-mail: hjyan@scu.edu.cn; Tel: +86-1355-1341-892

without further purification. The square-like WO_3 nanoplates were synthesized by hydrothermal synthesis method as follows: 1.0 g of $Na_2WO_4 \cdot 2H_2O$ was dissolved in 20 mL deionized water under constant stirring. Then, hydrochloric acid solution (5–6 mL, HCl : H_2O = 1 : 1 v/v) was added into the solution drop by drop and magnetically stirred for 30 minutes. The obtained yellow precipitate was washed thoroughly with distilled water for removing Cl^-, and then transferred into a 30 mL of Teflon-lined stainless steel autoclave for hydrothermal treatment at 180 °C for 24 h. As a result, the yellow precipitates were collected by centrifugation and washed with deionized water for several times and dried at 60 °C for overnight.

2.1.2 The deposition of Pt and metal oxide nanoparticles (MnO_x, RuO_2, CoO_x, and PbO_x) on WO_3 powder. Pt and metal oxide (MnO_x, CoO_x, and PbO_x) nanoparticles except RuO_2 were deposited on the WO_3 samples by photodeposition. For Pt/WO_3 preparation, the Pt cocatalysts were loaded onto WO_3 by photoreduction method in which 0.500 g of WO_3 powder was suspended in 200 mL aqueous methanol (10% in volume) containing defined amounts of $H_2PtCl_6 \cdot 6H_2O$. The resulting suspension was then stirred and illuminated for 0.5 h with a Xe lamp after removing the dissolved oxygen completely. The suspension was collected, washed with deionized water and ethanol for several times, and finally dried at 60 °C for overnight.

The photo-deposition of the PbO_x was achieved with $Pb(NO_3)_2$ as the precursor. For PbO_x/WO_3 preparation, 0.500 g of WO_3 powder and appropriate amount of $Pb(NO_3)_2$ were suspended in 200 mL H_2O solution with different pH values by the addition of nitric acid. After photoirradiation for 1 h, the resulting suspension was centrifuged, washed with deionized water and ethanol for several times, and finally dried at 60 °C for overnight. Pt/PbO_x/WO_3 was prepared using the similar method by loading PbO_x nanoparticles on the as-prepared platinized WO_3 powder (Pt/WO_3).

The photo-deposition of MnO_x or CoO_x was achieved with $MnSO_4$ or $Co(NO_3)_2$ as the precursor, and $NaIO_3$ was employed as the electron acceptor. Briefly, 0.500 g of WO_3 powder was suspended in 200 mL 0.01 M $NaIO_3$ aqueous solution containing a certain amount of $MnSO_4$ or $Co(NO_3)_2$. Then the mixture was illuminated with a Xe lamp for an hour under stirring after removing the dissolved oxygen completely. The product was collected, washed with deionized water and ethanol for several times, and finally dried at 60 °C for overnight.

RuO_2 was loaded by an impregnation method by using $Ru_3(CO)_{12}$ as the precursor according to the method presented previously.[24] Typically, WO_3 powder was immersed in a tetrahydrofuran (THF) solution containing appropriate amount of dissolved $Ru_3(CO)_{12}$ and stirred at 333 K for 6 h for 4–5 h. The samples were finally evaporated to dryness and calcined in air at 623 K for 5 h to convert the Ru species to RuO_2. The amount of RuO_2 loaded was 0.1 wt%.

2.2 Photocatalytic reactions

The photocatalytic water splitting O_2 evolution reactions were performed in a top-irradiation reactor vessel connected to a glass closed gas circulation system. The evolved gases were analyzed by an online gas chromatograph equipped with a thermal conductivity detector (SPSIC, GC-112AT, argon carrier). Typically, 0.300 g of the as-prepared photocatalyst was dispersed in 200 mL of 0.01 M aqueous $AgNO_3$ solution ($AgNO_3$ acts as the sacrificial reagent). Before irradiated by a 300 W Xe lamp without cutoff filter, the reaction mixture was evacuated for 1 h to completely remove air and establish the adsorption–desorption equilibrium between the solution and photocatalyst with a constant magnetic stirring. The temperature of the reaction solution was maintained at 283 K by a flow of cooling water during the reaction. The gas generated was analyzed every 1 h.

2.3 Characterization

Scanning electron microscope (SEM) images of the samples was performed with JSM-5900LV Scanning Electron Microscopy (SEM, JEOL, Japan). Transmission electron microscopy images (TEM), high-resolution (HR) TEM images of the samples were obtained on transmission electron microscope (TEM; Tecnai G2 F20 S-TWIN). Powder X-ray diffraction (XRD) patterns were obtained using a X-Pert Pro diffractometer with Cu Kα radiation (λ = 1.5406 Å) at a scanning speed of 4° min^{-1}. The UV-vis diffuse reflectance absorption spectra (DRS) were recorded on a UV-vis spectrophotometer (UV3600, Shimadzu) by using $BaSO_4$ as a reference. The photoluminescence (PL) spectra of the samples was carried out with a Hitachi F-7000 photoluminescence spectrophotometer (Hitachi F-7000) and the excitation wavelength was 230 nm. X-ray photoelectron spectroscopy (XPS) spectra were measured on a V4105 instrument (Thermo Electron, USA) with a Mn Kα radiation source.

3. Result and discussion

Fig. 1 shows the SEM image of square-like WO_3 nanoplates synthesized by hydrothermal method. The size of the WO_3 nanoplates was between several hundred nanometres and micrometres in length with a thickness of approximately 15–20 nm. The rectangular square-like WO_3 nanoplate with predominant facets of (002) and side facets of (020) and (200) based on our recent works.[23] It is known that Pt was used as the

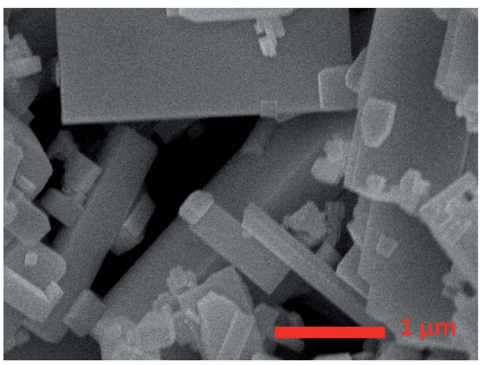

Fig. 1 SEM image of as-prepared square-like WO_3.

powerful reduction cocatalysts for high activity WO_3.[5,25] The choice of suitable oxidation cocatalysts is another important factor for photocatalytic water oxidation reaction. Fig. 2 shows the photocatalytic water oxidation activities of WO_3 loaded with different oxidation cocatalysts when platinum is fixed as the reduction cocatalyst. Four metal oxides, MnO_x, RuO_2, CoO_x, and PbO_x, known as water oxidation cocatalysts, can catalyze the water oxidation reactions to enhance the photocatalytic oxygen evolution of WO_3.[26–28] MnO_x, CoO_x, PbO_x, and Pt were deposited by photo-deposition method except that RuO_2 was deposited by the impregnation method. The photocatalytic O_2 evolution rate over WO_3 loaded with MnO_x, RuO_2, CoO_x or PbO_x is 446.8, 490.6, 636.7, 929.7 μmol h^{-1} g^{-1}, respectively. The activity order is MnO_x < RuO_2 < CoO_x < PbO_x. Compared to O_2 evolution rate of Pt/WO_3 (479.1 μmol h^{-1} g^{-1}), the photocatalytic activity of Pt–MnO_x/WO_3 was lower than Pt/WO_3, indicating that the MnO_x have less contribution to the O_2 evolution of WO_3. Almost very little improvement of photocatalytic activity was observed when RuO_2 was deposited. CoO_x show more effect on the enhanced photocatalytic activity than RuO_2. The water oxidation activity was increased much more obvious when PbO_x is used as the oxidation cocatalyst, suggesting that the loading of PbO_x and Pt as cocatalysts together shows a synergistic effect in photocatalysis.

The band edge position for WO_3 and some metal oxides are shown in Fig. 3. The electronic structures of PbO and Pb_3O_4 have been relatively well understood, while the band structure and the nature of metallic behaviour of PbO_2 are still controversial in recent years.[29] Therefore the band gap of PbO_2 is not listed in Fig. 3. The photogenerated holes in the valence band (VB) of WO_3 can be transfer to metal oxides, since the VB potential of WO_3 is more positive than that of metal oxides. The different activities of MO_x/Pt/WO_3 (M = Co, Ru, Pb, Mn) may be ascribed to the different matching degrees of energy band level and electronic structures between WO_3 and metal oxides.[22,30,31] It is known that the cocatalyst and semiconductor should have compatible lattice and electronic structures with suitable Fermi-levels or band levels, thus the migration of photogenerated carriers can be promoted by the internal field at the interface.[22,30,31] Furthermore, the processing condition and method of preparation metal oxides catalyst also play major roles in the stability, crystallinity, and the size of metal oxides particles, which are greatly affect the activities of catalysts.[32] Possible differences in roughness factors also can contribute to difference in performance of as-prepared samples. For example, stability for RuO_2, the size of CoO_x particles affects photocatalytic activity of photocatalyst.[33,34]

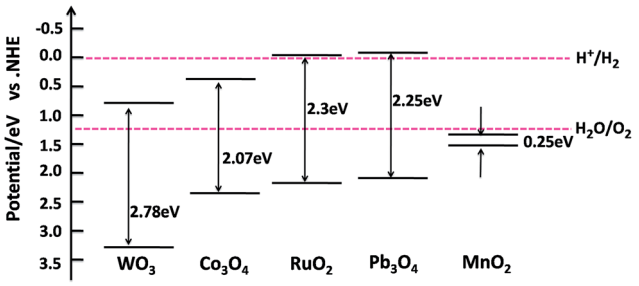

Fig. 3 Band structures of WO_3 and related transition metal oxides. Reference: WO_3,[2] MnO_2,[35,36] Co_3O_4,[31] Pb_3O_4,[37,38] RuO_2.[39–41]

Photo-oxidation deposition of PbO_x on WO_3 was prepared by using $Pb(NO_3)_2$ as the precursor in solution with different acidity. Fig. 4 shows the effect of the different acidity condition of loading PbO_x on photocatalytic activity over Pt/PbO_x/WO_3. The pH values were 1.8, 2.4, 3.77, 4.8, and 7 in the order from small to large. It clearly shows that the highest activity of Pt/PbO_x/WO_3 was observed at approximately pH in the range of 2 to 4. In order to clarify the influence of acidity on the photocatalytic activity, PbO_x/WO_3 (0.5 wt%, Pb) samples prepared by photooxidative deposition of PbO_x at three different pH values of 1.8, 2.4 and 4.8 were selected to characterize by X-ray photoelectron spectroscopy (XPS). The survey XPS spectrum (Fig. 5a) shows that the main elements on the surface of the composite were W, O, Pb and C. The C 1s peak observed in the survey scan is due to the carbon contamination which was used to calibrate the binding energy. For PbO_x/WO_3 samples prepared at pH values of 1.8 and 2.4, the peaks locates at around

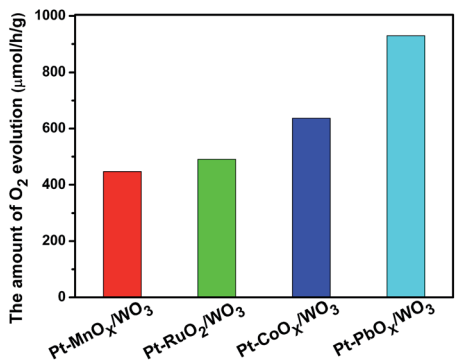

Fig. 2 Photocatalytic water oxidation activities of WO_3 loaded with different oxidation cocatalysts and Pt as the reduction cocatalyst. The amount of Pt and metal oxide nanoparticles cocatalysts were all set to be 0.5 wt% and 0.1 wt% respectively.

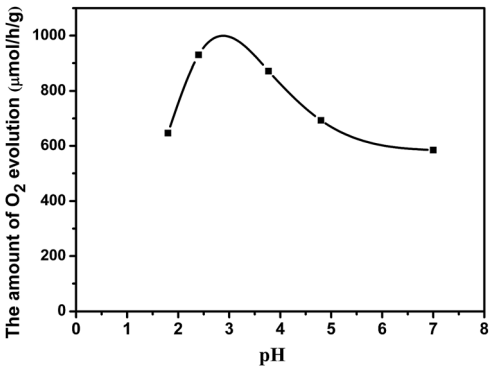

Fig. 4 Photocatalytic water oxidation activities over Pt/PbO_x/WO_3, where the PbO_x was loaded in solution with different acidity condition. The amount of Pt and PbO_x nanoparticles cocatalysts were set to be 0.5 wt% and 0.1 wt% respectively.

35.50 and 37.61 eV (see Fig. 5b), related to W $4f_{7/2}$ and W $4f_{5/2}$ binding energies of W(VI) oxidation state in the tungsten oxide sample.[8,26] The O 1s peak (Fig. 5c) at 530.30 eV is associated with the lattice oxygen in WO_3, and the other peak at 531.97 eV corresponds with surface adsorbed hydroxide and water.[8,26,42,43]

The Pb 4f spectrum for PbO_x/WO_3 sample prepared at pH value of 2.4 exhibited two binding energies at 138.80 and 143.64 eV, corresponding to Pb $4f_{7/2}$ and Pb $4f_{5/2}$ for Pb^{4+}, respectively. This result indicated that PbO_2 was formed when the PbO_x was loaded at pH value of 2.4.[26,42–46] For PbO_2/WO_3 sample prepared at pH values of 4.8 (near neutral pH), the Pb 4f spectrum exhibited two peaks at 138.95 and 143.85 eV, corresponding to Pb $4f_{7/2}$ and Pb $4f_{5/2}$ in the form of Pb_3O_4,[42,47,48] respectively, which indicated both states of Pb(II) and Pb(IV) exist in this photocatalyst. With the increase in acidity, nitric acid will gradually dissolve lead oxide to produce Pb^{2+}, then the Pb^{2+} was oxidized by photo-generated holes ($Pb^{2+} + 2H_2O + 2h^+ = PbO_2 + 4H^+$). The increased peak intensity of Pb observed in the XPS of sample with pH value of 2.4 suggests that solution pH not only affect the chemical states of Pb in PbO_x but also affect the loading amount of PbO_x. Therefore, the different photocatalytic performances (as shown in Fig. 4) of $Pt/PbO_x/WO_3$ prepared by pH values of 2.4 and 1.8 may be caused by the loading amount of PbO_x, and the different performances of $Pt/PbO_x/WO_3$ prepared at pH = 2.4 to 7 may be caused by the slow change of valence states of lead in loaded oxides of lead. Compared to the samples prepared at pH values of 2.4 and 1.8, the W 4f and O 1s peaks of PbO_x/WO_3 sample prepared at near neutral pH (pH 4.8) show a small shift about 0.2 eV toward high binding energy, which could be due to the effect of states in the loaded PbO_x.

The XRD patterns of the prepared catalysts are shown in Fig. 6. The patterns clearly demonstrated that the pure WO_3 exhibits a monoclinic phase structure with obvious characteristic diffraction peaks at 2θ values of 23.15, 23.61, 24.37, 33.30, and 34.19°, corresponding to the (002), (020), (200), (022) and (202) planes, respectively (JCPDS no. 72-1465, a = 7.300 Å, b = 7.530 Å, and c = 7.680 Å). All samples have monoclinic WO_3 structure and the cocatalysts loading does not influence the crystal structures of WO_3. In the XRD patterns of Pt/WO_3, and $Pt/PbO_x/WO_3$ samples, no related peaks of Pt or PbO_x except for monoclinic WO_3 are observed because of the tiny amount of Pt(0.5 wt%), PbO_x(0.1 wt%), small size and high dispersion in the samples.

The morphology of square-like WO_3 deposited with Pt cocatalyst (0.5 wt%) was observed, and the SEM and TEM image was shown in Fig. 7a and b, respectively. Obviously, Pt nanoparticles with a primary size of 2–3 nm were mainly deposited on the side (020) and (200) facets of the square-like WO_3 nanoplates and seriously aggregated. The phenomenon of preferred deposition of Pt is due to intrinsic differences in surface charge of square-like WO_3 nanoplates leading sorption-induced deposition of Pt on square-like WO_3.[49] Prior to photoreduction, since the edges appear positively charged and then preferentially adsorb the negatively charged $[PtCl_6]^{2-}$ ions, thus leading to the observed sorption-determined preferred deposition of platinum on the edged facets of square-like WO_3.[49] Fig. 7c shows the SEM image of WO_3 deposited with PbO_x (Pb, 0.1 wt%) by photo-oxidation deposition method. As shown in Fig. 7c, PbO_x with size of more than 5 nm were mainly loaded on the dominant (002) facets of square-like WO_3, while almost no PbO_x particles were observed on the side (020) and (200) facets.

The TEM and SEM images of the square-like WO_3 deposited with Pt and PbO_x dual cocatalysts by *in situ* photo-reduction and photo-oxidation deposition methods were also obtained and are shown in Fig. 8. The HRTEM image (Fig. 8d) shows that the lattice fringes of nanoparticles on side (020) and (200) facets is 0.227 nm, which can be indexed to the (111) plane of Pt (JCPDS, no. 70-2431), and it is also hard to find out the PbO_x on the side (020) and (200) facets of square-like WO_3. As shown in Fig. 8a, it is clearly observed that the surface of tungsten trioxide including the small and dominant facets are covered with cocatalysts. PbO_x and Pt can be easily discerned through the particle sizes. Combining both the TEM and SEM images shown

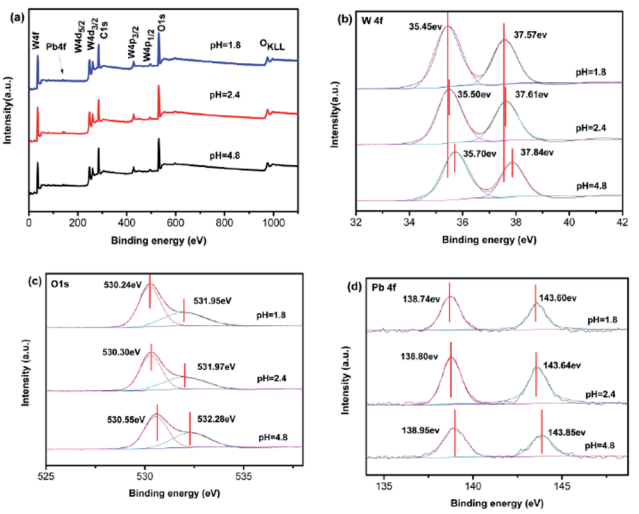

Fig. 5 The XPS survey scan (a), and the corresponding high-resolution XPS spectra of W 4f (b), O 1s (c), and Pb 4f (d) of PbO_x/WO_3 samples prepared by photo-deposition at different acidity.

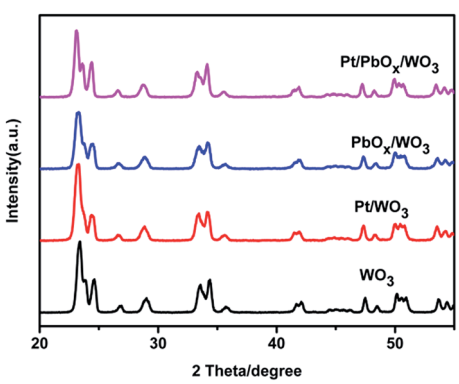

Fig. 6 The X-ray diffraction (XRD) patterns of as-synthesized WO_3, Pt/WO_3, PbO_x/WO_3 and $Pt/PbO_x/WO_3$ samples. PbO_x in the samples were loaded at pH = 3.77.

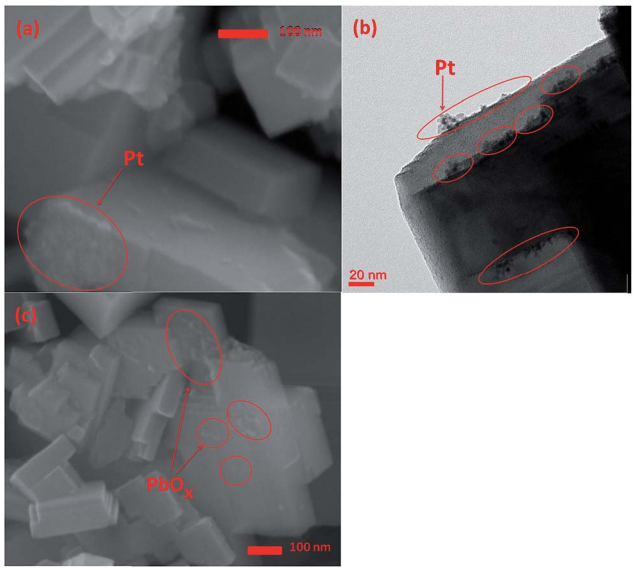

Fig. 7 SEM image (a) and TEM image (b) of as-prepared Pt/WO_3, and SEM image of PbO_x/WO_3 prepared at pH = 2.4 (c).

in Fig. 7 and 8, we can clearly confirm that the PbO_x nanoparticles with a diameter of around 5–10 nm are selectively deposited on the dominant (002) facets of square-like WO_3, while Pt nanoparticles with smaller particle size were deposited on the side (020) and (200) facets of square-like WO_3. Considering that the basal (002) planes indicates a weak negative surface charge,[49] dark sorption of the positively charged Pb^{2+} ions prior to photoreduction is probably preferred at the dominant (002) facets rather than positively charged edges. When illumination, light-induced spatial separation of the photogenerated electrons and holes toward the edged facets and the dominant crystal facets of square-like WO_3 nanoplates, respectively.[23] The photogenerated holes that directional migration to (002) facets will oxidize the divalent lead ions to

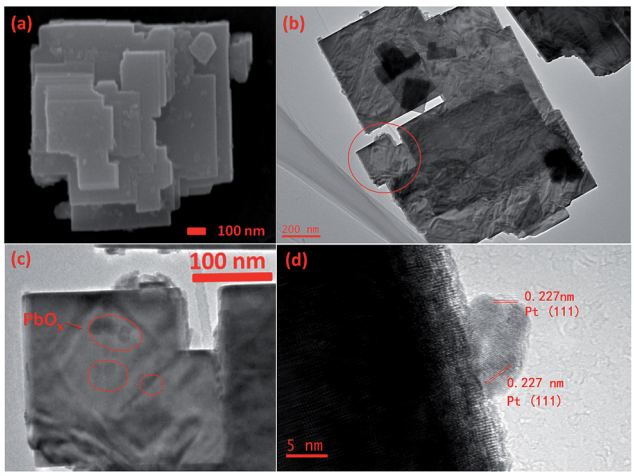

Fig. 8 SEM image (a), TEM image (b), and HRTEM (d) images of $Pt/PbO_x/WO_3$, on which PbO_x was loaded at pH = 2.4. The enlargement TEM image of circle part in (b) is shown in (c).

PbO_x, thus resulting in preferred loading of PbO_x on the dominant planes of WO_3.

As shown in Fig. 9, the photocatalytic oxygen evolution activity is strongly dependent on the cocatalysts photodeposited on the surface of the square-like WO_3. The highest water oxidation activity is achieved for the $Pt/PbO_x/WO_3$ sample with metallic platinum and PbO_x particles selectively photodeposited on the edged and dominant facets, respectively. The rate of O_2 evolution on Pt/WO_3 and PbO_x/WO_3 is 479.1 μmol h^{-1} g^{-1} and 599.0 μmol h^{-1} g^{-1}, respectively. Loading PbO_x on the dominant (002) facets of WO_3 can enhance the photocatalytic O_2 evolution rate further. However, the O_2 evolution rate on $Pt/PbO_x/WO_3$ is 929.7 μmol h^{-1} g^{-1}. The photocatalytic water oxidation activity of $Pt/PbO_x/WO_3$ is nearly double than that of Pt/WO_3, indicating that PbO_x nanoparticles located on the dominant facets of square-like WO_3 have a positive effect on water oxidation reaction.

As demonstrated in Fig. 10, the UV-vis diffuse reflectance spectra of the square-like WO_3 loaded with different cocatalysts show similar absorption property to pure WO_3 with a strong absorption range from 200 to 350 nm, but slightly weakened the absorption intensity due to that the cocatalysts shadow the photocatalyst absorbing the light.[50] It can be deduced from the adsorption edge that all the samples has a band gap of 2.78 eV, indicating that the loaded of PbO_x and Pt on the surface of square-like WO_3 did not change its band gap. The photoluminescence spectra (Fig. 11) of the photocatalysts give more information of the density of recombination of photogenerated electron–hole pairs. Pt/WO_3 and PbO_x/WO_3 exhibit weaker emission peak intensity than pure WO_3 and a significantly decreased PL intensity is observed for $Pt/PbO_x/WO_3$ in the wavelength range of 300–800 nm, suggesting that the lower electron–hole recombination rate in $Pt/PbO_x/WO_3$.[51] The result of PL is in good agreement with that of photocatalytic performances (Fig. 9). Such a decreased electron–hole recombination might be ascribed to selective deposition of a suitable dual-cocatalysts onto the needed facets of square-like WO_3 leading accelerated transfer of the photogenerated electrons and holes from the surfaces of WO_3.

It has been reported that the deposition of suitable dual-cocatalysts on the needed facets of semiconductor-based

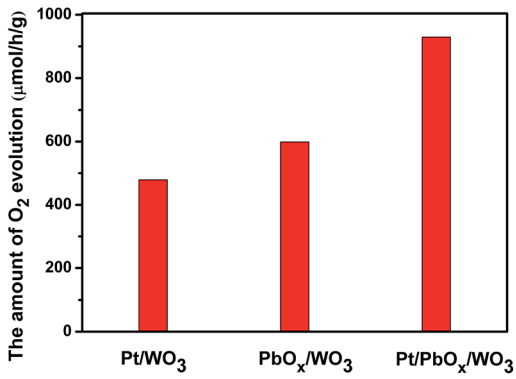

Fig. 9 Photocatalytic water oxidation performances of Pt/WO_3 and $Pt/PbO_x/WO_3$.

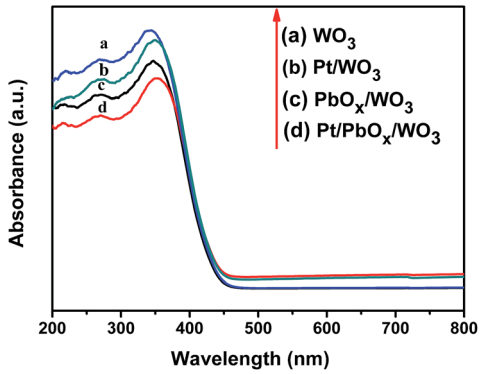

Fig. 10 PL spectra of WO_3, Pt/WO_3, PbO_x/WO_3 and $Pt/PbO_x/WO_3$.

crystals (*e.g.*, $BiVO_4$, TiO_2) resulted in a remarkable synergetic effect in the photocatalytic performance, which could be attributed to the spatial separation of the photogenerated charges between facets.[13,16,22] Our recent research works reveal that light-induced preferential flow of photogenerated holes and electrons to the dominant (002) facets and edged facets of square-like WO_3, on which oxidation and reduction occurs, respectively.[23] Here we proposed the reaction mechanism of visible-light-driven O_2 evolution over the square-like WO_3 loaded with Pt and PbO_x dual cocatalysts as depicted in Fig. 12. PbO_x nanoparticles dispersed on the hole-rich (002) facets were function as oxidation cocatalysts for trapping holes where as Pt nanoparticles dispersed on the electron-rich (020) and (200) facets were function as reduction cocatalysts for trapping electrons. In general, light-induced spatial separation of the photogenerated electrons and holes toward the edged facets and the dominant crystal facets of square-like WO_3 nanoplates respectively, which results in hole-rich (002) major top facets and electron-rich (020) and (200) facets.[23] The oxidation reaction of water to O_2 evolution takes place on the hole-rich (002) major top facets, while the reduction reaction takes place on the electron-rich (020) and (200) facets. At the same time, PbO_x cocatalysts loaded on the dominant facets act as oxidation sites for O_2 evolution to catalyze the four-electron water oxidation to produce O_2, Pt loaded on the edged facets are to offer reduction sites for Ag^+ and catalyze the reduction reactions, namely the

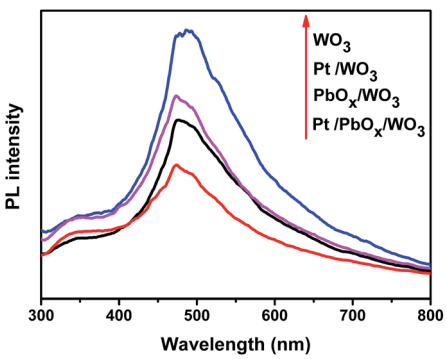

Fig. 11 UV-vis diffuse reflectance spectra of WO_3, Pt/WO_3, PbO_x/WO_3 and $Pt/PbO_x/WO_3$.

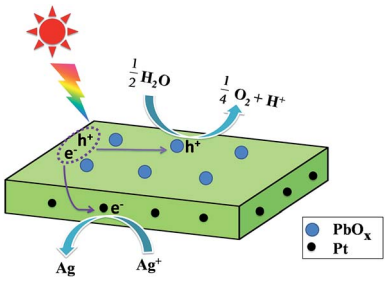

Fig. 12 Proposed mechanism of photocatalytic water splitting O_2 evolution over $Pt/PbO_x/WO_3$ photocatalyst.

reduction of Ag^+ to Ag. The simultaneous existence of Pt and PbO_x cocatalysts is supposed to be synergistically working for the efficient separation and transfer of the photoexcited electrons and holes, thus contributing to the photocatalytic performance of $Pt/PbO_x/WO_3$.

4. Conclusion

In conclusion, square-like WO_3 nanoplates with specific exposed crystal facets were synthesized by hydrothermal method. Pt and PbO_x dual cocatalysts were selectively deposited on the edged (200) and (020) facets and the dominant (002) facets of square-like WO_3 by photo-deposited, respectively. The WO_3 deposited with dual cocatalysts show remarkable enhanced photocatalytic activities than that WO_3 loaded with single cocatalyst. The enhanced photocatalytic performances are due to light-induced spatial separation of the photogenerated electrons and holes toward different facets of square-like WO_3 nanoplates and selectively deposition of suitable dual-cocatalysts onto the needed facets of square-like WO_3.

Acknowledgements

We thank the National Natural Science Foundation of China (No. 21273157) for the financial support.

References

1 B. Ma, J. Kim, T. Wang, J. Li, K. Lin, W. Liu and S. Woo, *RSC Adv.*, 2015, **5**, 79815–79819.
2 J. Zhang, Z. Liu and Z. Liu, *ACS Appl. Mater. Interfaces*, 2016, **8**, 9684–9691.
3 X. Xiang, L. Zhang, L. Chou and X. Li, *CrystEngComm*, 2014, **16**, 5180.
4 M. Liu, H. Li and Y. Zeng, *J. Nanomater.*, 2015, **2015**, 1–7.
5 H. Widiyandari, A. Purwanto, R. Balgis, T. Ogi and K. Okuyama, *Chem. Eng. J.*, 2012, **180**, 323–329.
6 K. Kalantar-zadeh, J. Z. Ou, T. Daeneke, A. Mitchell, T. Sasaki and M. S. Fuhrer, *Applied Materials Today*, 2016, **5**, 73–89.
7 J. Z. Ou, R. A. Rani, S. Balendhran, A. S. Zoolfakar, M. R. Field, S. Zhuiykov, A. P. O'Mullane and K. Kalantar-zadeh, *Electrochem. Commun.*, 2013, **27**, 128–132.
8 Y. Feng, C. Liu, H. Che, J. Chen, K. Huang, C. Huang and W. Shi, *CrystEngComm*, 2016, **18**, 1790–1799.

9 W. Shi, H. Lv, S. Yuan, H. Huang, Y. Liu and Z. Kang, *Sep. Purif. Technol.*, 2017, **174**, 282–289.
10 P. Wang, Y. Xia, P. Wu, X. Wang, H. Yu and J. Yu, *J. Phys. Chem. C*, 2014, **118**, 8891–8898.
11 G. W. Busser, B. Mei, P. Weide, P. C. K. Vesborg, K. Stührenberg, M. Bauer, X. Huang, M.-G. Willinger, I. Chorkendorff, R. Schlögl and M. Muhler, *ACS Catal.*, 2015, **5**, 5530–5539.
12 D. Noureldine, D. H. Anjum and K. Takanabe, *Phys. Chem. Chem. Phys.*, 2014, **16**, 10762–10769.
13 L. Mu, Y. Zhao, A. Li, S. Wang, Z. Wang, J. Yang, Y. Wang, T. Liu, R. Chen, J. Zhu, F. Fan, R. Li and C. Li, *Energy Environ. Sci.*, 2016, **9**, 2463–2469.
14 Y. Ma, R. Chong, F. Zhang, Q. Xu, S. Shen, H. Han and C. Li, *Phys. Chem. Chem. Phys.*, 2014, **16**, 17734–17742.
15 Q. Zhang, Z. Li, S. Wang, R. Li, X. Zhang, Z. Liang, H. Han, S. Liao and C. Li, *ACS Catal.*, 2016, **6**, 2182–2191.
16 Q. Zhang, R. Li, Z. Li, A. Li, S. Wang, Z. Liang, S. Liao and C. Li, *J. Catal.*, 2016, **337**, 36–44.
17 T. Tanabe, W. Miyazawa, T. Gunji, M. Hashimoto, S. Kaneko, T. Nozawa, M. Miyauchi and F. Matsumoto, *J. Catal.*, 2016, **340**, 276–286.
18 E. Bae and T. Ohno, *Appl. Catal., B*, 2009, **91**, 634–639.
19 L. Zhang, W. Wang, S. Sun, D. Jiang and E. Gao, *Appl. Catal., B*, 2015, **162**, 470–474.
20 C. Zhen, J. C. Yu, G. Liu and H. M. Cheng, *Chem. Commun.*, 2014, **50**, 10416–10419.
21 A. Meng, J. Zhang, D. Xu, B. Cheng and J. Yu, *Appl. Catal., B*, 2016, **198**, 286–294.
22 R. Li, H. Han, F. Zhang, D. Wang and C. Li, *Energy Environ. Sci.*, 2014, **7**, 1369.
23 H. Gong, R. Ma, F. Mao, K. Liu, H. Cao and H. Yan, *Chem. Commun.*, 2016, **52**, 11979–11982.
24 K. Teramura, K. Maeda, T. Saito, T. Takata, N. Saito, Y. Inoue and K. Domen, *J. Phys. Chem. B*, 2005, **109**, 21915–21921.
25 K. Wenderich and G. Mul, *Chem. Rev.*, 2016, **116**, 14587–14619.
26 S. Anandan and M. Miyauchi, *Chem. Commun.*, 2012, **48**, 4323–4325.
27 S. S. K. Ma, K. Maeda, R. Abe and K. Domen, *Energy Environ. Sci.*, 2012, **5**, 8390.
28 C. S. Chua, D. Ansovini, C. J. Lee, Y. T. Teng, L. T. Ong, D. Chi, T. S. Hor, R. Raja and Y. F. Lim, *Phys. Chem. Chem. Phys.*, 2016, **18**, 5172–5178.
29 F. Ma, Y. Jiao, G. Gao, Y. Gu, A. Bilic, S. Sanvito and A. Du, *ACS Appl. Mater. Interfaces*, 2016, **8**, 25667–25673.
30 J. Yang, D. Wang, H. Han and C. Li, *Acc. Chem. Res.*, 2013, **46**(8), 1900–1909.
31 M. Long, W. Cai, J. Cai, B. Zhou, X. Chai and Y. Wu, *J. Phys. Chem. B*, 2006, **110**(41), 20211–20216.
32 M. G. Walter, E. L. Warren, J. R. McKone, *et al.*, *Chem. Rev.*, 2010, **110**(11), 6446–6473.
33 C. Iwakura and H. Tamura, *Int. J. Hydrogen Energy*, 1982, **7**, 857.
34 L. Liu, X. Gu, C. Sun, H. Li, Y. Deng, F. Gao and L. Dong, *Nanoscale*, 2012, **4**, 6351.
35 Y. Xu and M. A. A. Schoonen, *Am. Mineral.*, 2000, **85**, 543–556.
36 A. K. M. Farid Ul Islam, R. Islam and K. A. Khan, *J. Mater. Sci.: Mater. Electron.*, 2005, **16**(4), 203–207.
37 E. Ayalew, K. Janssens and K. D. Wael, *Anal. Chem.*, 2016, **88**(3), 1564–1569.
38 Y. Zhou, J. Long, Q. Gu, H. Lin, H. Lin and X. Wang, *Inorg. Chem.*, 2012, **51**, 12594–12596.
39 M. T. Uddin, Y. Nicolas, C. Olivier, T. Toupance, M. M. Müller, H. J. Kleebe, K. Rachut, J. Ziegler, A. Klein and W. Jaegermann, *J. Phys. Chem. C*, 2013, **117**, 22098–22110.
40 B. H. Tan, E. Ye and W. Y. Fan, *Adv. Mater.*, 2006, **18**, 619–623.
41 A. K. Goel, G. Skorinko and F. H. Pollak, *Phys. Rev. B: Condens. Matter Mater. Phys.*, 1981, **24**, 7342.
42 J. M. Thomas and M. J. Tricker, *J. Chem. Soc., Faraday Trans. 2*, 1975, **71**, 329–336.
43 Y. Liu, H. Liu, J. Ma and J. Li, *Electrochim. Acta*, 2011, **56**, 1352–1360.
44 M. Xu, Z. Wang, F. Wang, P. Hong, C. Wang, X. Ouyang, C. Zhu, Y. Wei, Y. Hun and W. Fang, *Electrochim. Acta*, 2016, **201**, 240–250.
45 X. Ma, R. Wang, W. Guo, H. Yang, Z. Liang and C. Fan, *Int. J. Electrochem. Sci.*, 2012, **7**, 6012–6024.
46 L. Lubenov, M. Bojinov and T. Tzvetkoff, *J. Solid State Electrochem.*, 2007, **11**, 1613–1620.
47 K. S. Kim, T. J. O'Leary and N. Winograd, *Anal. Chem.*, 1973, **45**(13), 2214–2218.
48 K. I. B. Eguiluz, G. R. P. Malpass, M. M. S. Pupo, G. R. Salazar-Banda and L. A. Avaca, *Energy Fuels*, 2010, **24**, 4012–4024.
49 K. Wenderich, A. Klaassen, I. Siretanu, F. Mugele and G. Mul, *Angew. Chem., Int. Ed.*, 2014, **53**, 12476–12479.
50 C. Young, T. M. Lim, K. Chiang, J. Scott and R. Amal, *Appl. Catal., B*, 2008, **78**, 1–10.
51 Y. Zhang, F. Mao, H. Yan, K. Liu, H. Cao, J. Wu and D. Xiao, *J. Mater. Chem. A*, 2015, **3**, 109–115.